LAWRENCE
LIVERMORE
NATIONAL
LABORATORY

UCRL-JRNL-205451

Axial and Temporal Gradients in Mo Z Pinches

P. D. LePell, S. B. Hansen, A. S. Shlyaptseva, C. Coverdale, C. Deeney, J. P. Apruzese, K. B. Fournier, U. I. Safronova

July 23, 2004

Physics of Plasmas

Disclaimer

This document was prepared as an account of work sponsored by an agency of the United States Government. Neither the United States Government nor the University of California nor any of their employees, makes any warranty, express or implied, or assumes any legal liability or responsibility for the accuracy, completeness, or usefulness of any information, apparatus, product, or process disclosed, or represents that its use would not infringe privately owned rights. Reference herein to any specific commercial product, process, or service by trade name, trademark, manufacturer, or otherwise, does not necessarily constitute or imply its endorsement, recommendation, or favoring by the United States Government or the University of California. The views and opinions of authors expressed herein do not necessarily state or reflect those of the United States Government or the University of California, and shall not be used for advertising or product endorsement purposes.

Axial and temporal gradients in Mo Z pinches

P. D. LePell
Sandia National Laboratories, Albuquerque, New Mexico 87185

S. B. Hansen
University of Nevada, Reno, Physics Department/220, Reno, Nevada, 89557 and
Lawrence Livermore National Laboratory, Livermore, CA 94551

A. S. Shlyaptseva
University of Nevada, Reno, Physics Department/220, Reno, Nevada, 89557

C. Coverdale and C. Deeney
Sandia National Laboratories, Albuquerque, New Mexico 87185

J. P. Apruzese
Radiation Hydrodynamics Branch, Plasma Physics Division, Naval Research Laboratory,
Washington, D.C. 20375

K. B. Fournier
Lawrence Livermore National Laboratory, Livermore, CA 94551

U. I. Safronova
University of Notre Dame, Notre Dame, IN 46566

Three nested molybdenum wire arrays with initial outer diameters of 45, 50, and 55 mm were imploded by the ~ 20 MA, 90 ns rise-time current pulse of Sandia's Z accelerator. The implosions generated Mo plasmas with approximately 10% of the array's initial mass reaching Ne-like and nearby ionization stages. These ions emitted 2 – 4 keV L-shell x-

rays with radiative powers approaching 10 TW. Mo L-shell spectra with axial and temporal resolution were captured and have been analyzed using a non-LTE collisional-radiative model. We find significant axial variation in the plasma conditions, with electron densities increasing from the cathode (~ 3 x $10^{20}$$cm^{-3}$) to near the anode end of the plasma (~ 3 x $10^{21}$$cm^{-3}$) and electron temperatures decreasing slightly from the cathode (~ 1.7 keV) to the anode end (~ 1.5 keV). Time-resolved spectra indicate that the peak electron density is reached before the peak of the L-shell emission and decreases with time, while the electron temperature remains within 10% of 1.7 keV over the 20 - 30 ns L-shell radiation pulse. Finally, while the total yield, peak total power, and peak L-shell power all tended to decrease with increasing initial wire array diameters, the L-shell yield and the average plasma conditions varied little with the initial wire array diameter. Radiative cooling is likely to play an important role in the wire array plasma development.

52.25.Os, 52.70.La, 32.30.Rj, 32.70.Fw

I. INTRODUCTION

Ultra-fast, pulsed-power-driven Z-pinches have been studied extensively as sources of 1 – 3 keV x-rays [1 2 3 4 5] and have recently been investigated as sources of 3 – 6.7 keV x-rays on the Z accelerator. [6 7 8] These x-rays have been produced by heating low-atomic-number materials ($10 < Z < 28$) to high temperatures at which the ionization stages are predominantly in the K-shell. During the 1990s, a large body of theoretical work focused on how to ensure that K-shell ionization could be achieved and how the x-ray yields would scale for different materials and driver currents. [9 10] Several major issues were identified that could limit the production of higher-energy x-ray emissions: First, the higher velocities needed to ionize materials with $Z > 18$ require large increases in imploded mass and density to ensure efficient thermalization and collisional pumping of the excited states. [9 10] Second, the larger array diameters needed to achieve higher implosion velocities increase the risks associated with implosion instabilities and large

wire-to-wire separations. [7 11 12 13 14 15 16 17] Finally, materials with higher atomic numbers will have increased radiation loss rates from the L- and M-shells. [9] These increased radiation losses can cool the plasma, making K-shell ionization more difficult. Consequently, understanding the production of the L- and M-shell emission is important in the development of mid-Z K-shell sources.

An alternate approach to making x-rays sources with > 3 keV photon energies is to generate L-shell emission from materials with higher atomic numbers ($30 < Z < 47$). L-shell emission has some intrinsic advantages over K-shell emission: the numerous radiative channels in the L-shell might mitigate the effects of self-absorption, which can be significant in K-shell wire array implosions, [18] and there is little danger of stripping L-shell ions with ten or so electrons to bare ions that lack any strong radiative emission channel. However, as discussed in [19], L-shell radiators require more energy per ion than K-shell radiators due to the larger number of electrons that must be stripped off and heated to the requisite temperature. Table 1, which gives the minimum kinetic energy per ion required to produce L- and K-shell x-rays of given energies, shows that L-shell radiators require about 2.6 times more energy per ion than equivalent photon-energy K-shell radiators. For example, He-like Al has an ion charge of 11 and emits K-shell photons with energies near 1.7 keV, whereas Ne-like Kr, which emits L-shell x-rays of similar energy, has an ion charge of 26. Given equivalent electron temperatures, the required energy in the L-shell case is much higher, even without considering the energy expended in ionization.

To date, some experiments have been performed with L-shell radiators of Ni [20] and Kr, [21] but there has been little analysis of the stagnated plasma conditions. With the 20 MA Z accelerator, it is possible to implode wire arrays with masses greater than 1000 μg/cm; thus it was conceivable to implode Mo wire arrays using the minimum wire size of 13.5 μm (with 14.6 μg/cm per wire) with reasonable wire numbers. Based on the analysis given in [19], it was estimated that arrays 26 mm in diameter would be needed to achieve twice the minimum implosion velocities required to excite Mo in its L-shell. In fact,

implosions of wire arrays with greater than 40 mm diameters are achievable on Z with large masses and high wire numbers.

Mo wire array implosions on Z are interesting for a number of reasons: The 2 – 4 keV L-shell emission from Ne-like Mo and surrounding charge states [22] [23] brackets the ~ 3 keV K-shell emission from Ar, opening the opportunity to mix elements using wire arrays to obtain a broad x-ray emission spectrum for radiation-material interaction studies. In addition, these photon energies are accessible to crystal spectrometers, [24] x-ray diodes, [25] and photo-conducting detectors [26] and there is a substantial amount of Mo L-shell data from smaller devices, [27] [28] [29] some of which has already been analyzed using the present collisional-radiative L-shell model. [27] [29] [30] Another point of interest is whether the Mo Z pinch plasma achieves conditions that are of potential interest for x-ray laser studies: Ne-like Mo generated using a laser-plasma drive has been established as a high-gain (~ 4 cm^{-1}) medium for a collisionally-pumped x-ray laser. [31] The potential for lasing in Mo wire arrays on Z will be addressed in a future paper. Finally, as noted above, understanding heating and radiative cooling rates in the M- and L-shells is an important part of developing > 10 keV x-ray sources using K-shell emission from elements with $30 < Z < 50$. This has been shown for Kr using detailed radiation-magnetohydrodynamic (MHD) calculations. [32]

This paper describes a series of Mo wire array experiments conducted on the 20 MA Z accelerator at Sandia National Laboratories. [33] The experiments set out to investigate Z's potential to generate Mo L-shell x-rays and to determine optimum array configurations to maximize L-shell output. In addition, the time- and space-resolved spectroscopic measurements give insight into temperature and density gradients in the wire array implosions. Section II provides a description of the experiment and diagnostic instrumentation, including time-gated and axially resolved spectrometers. In Section III, the L-shell Mo model used to analyze the spectroscopic data is described. The results of the analysis are described in section IV and a comparison between the x-ray source properties of L-shell Mo and K-shell Ti and Ar are given in section V. A summary and our conclusions are given in Section VI.

II. EXPERIMENT AND MEASUREMENTS

Implosions on the Z accelerator of nested wire arrays of Al, Ti, and W [34 35] have generated high compression ratios and pulse widths a factor of two shorter than single arrays. The Mo arrays discussed here were composed of 13.5 μm-diameter Mo wires, had outer array diameters of 45, 50, and 55 mm, and had concentric inner arrays with diameters and wire numbers equal to half those of the outer arrays (the interwire gaps were therefore the same for the both the inner and outer arrays). The array configurations are detailed in Table 2 along with calculated 0-D implosion times, 0-D implosion velocities, and η values. (The η value is the ratio of the kinetic energy in the implosion to the minimum energy needed for production of L-shell x-rays (see Table 1) and has been deduced from 0-D estimates of the implosion velocity and an assumed compression ratio of 10:1.) In the 0-D calculations, a circuit model drives all of the array's initial mass. The value of η for each of the load designs exceeds 2, which was found to be the minimum η for efficient generation of K-shell x-rays (although there has been no experimental validation for L-shell radiators). It should also be noted that recent experiments and calculations indicate that the implosion dynamics for wire arrays do not follow 0-D behavior. In fact, some portions of the implosion probably have velocities slower than 0-D while others may have velocities greater than 0-D.

The Mo wire arrays were converted to plasma and imploded under the effects of Z's current pulse, which rose in these experiments to a peak of 18 MA in 85 – 90 ns, as shown in Fig. 1 (a) for the 50 mm diameter array. (In the sections that follow, selected data is presented only for the intermediate-diameter (50 mm) wire array whenever it is representative of the whole experimental series.) Figure 1 (a) also shows the broad-band x-ray pulse from this shot, which rose to a peak of 160 TW. Z's current heated and compressed the wire arrays to form hot, dense plasmas about 20 mm tall along the axis of the generator's diode with diameters of 1 – 3 mm. Figure 1 (b) shows a time sequence of pinhole images from a 5 mm region near the center portion of the plasma created by

imploding the 50 mm-diameter Mo wire array. The pinhole images indicate significant axial variations in the > 1 keV emission from the wire array implosion that are consistent with the variations in plasma conditions diagnosed from 2 – 4 keV L-shell emission (discussed in Section IV below).

A. Measurements of x-ray output

The x-ray outputs from the experiments were recorded with a variety of instruments that measured the power, energy, and spectral characteristics of the plasma radiation as well as the plasma's spatial extent and time history. Many of the detectors were filtered with thin layers of metal or polymers to tailor their response to discrete wavelength bands. In particular, Mo L-shell power was recorded using a set of diamond photo-conducting diodes (PCDs) filtered with 50.8 um of Kapton (giving 10% transmission at 2.1 keV) and L-shell yields were obtained by integrating these filtered PCD measurements over time. The total radiated energy (or yield) was measured with unfiltered, 1 μm-thick Ni-foil bolometers, and the total radiated power was determined by scaling the power pulse recorded by lightly filtered x-ray diodes (XRDs) to the energy measured by the bare bolometers. The XRDs were filtered with 4 μm of polycarbonate, which has a transmission notch at the carbon edge (277 eV) and 10% transmission at 800 eV.

Figure 2 shows the time histories of the L-shell and total radiated power from each of the three Mo wire arrays. The array with an initial diameter of 45 mm has a peak L-shell power approaching 10 TW, the largest L-shell power of the three arrays. The 50 mm array has a slightly smaller peak L-shell power, and the peak L-shell power of the 55 mm array is less than half that of the smallest array. (The L-shell emission pulse from the 55 mm array is significantly longer than the pulses from the smaller arrays and has three distinct peaks instead of one.) The largest-diameter array also had the smallest recorded peak total radiated power, which dropped to 80 TW from the 140 – 160 TW level measured for the 45 and 50 mm arrays.

The total radiated yield from the arrays fell from 1.66 to 1.16 MJ as the initial array diameter increased from 45 mm to 55 mm. However, the total L-shell yields did not indicate a strong dependence on the initial array diameter: all fell within 10% of 72 kJ and the highest L-shell yield was observed for the intermediate-diameter (50 mm) array. These results are summarized in Table 3. Overall, the largest-diameter array performed worse than the two smaller arrays. This might be due the large interwire gaps in the 55 mm array, which could lead to increased instabilities during the array implosion and can also permit increased amounts of cold precursor plasma to assemble on axis before the arrival of the majority of the array mass. Future experiments are needed to fully understand the nested array dynamics.

B. Spectroscopy of Mo Z-pinches

Four spectrometers were fielded to capture and disperse x-rays emitted from the Mo plasma, providing a wealth of detailed data over a wide spectral range. Each spectrometer used convex crystals as analysers. Three of the spectrometers used film as the detecting medium, and therefore were time-integrating. The fourth spectrometer used a gated micro-channel plate as the detector, providing time-resolution. Two of the time-integrating spectrometers were configured to capture the L-shell emission (ranging from 2 to 4 keV) from Ne-like Mo ions, which were expected to be the dominant species. In addition, because there was a small but finite possibility that some regions of the plasma could reach He-like conditions and because near Ne-like ions can undergo inner-shell excitation and emit 17 – 20 keV photons, the third time-integrating spectrometer was configured to capture any possible K shell emission above 15 keV.

The two time-integrating L-shell spectrometers were spatially resolved: one axially and the other radially. The time-resolved spectrometer and the high-energy spectrometer were not spatially resolved. The goal was to acquire as complete a data set as possible and to extract from the data knowledge of the structure and time-evolution of the Mo plasma. In this paper, we present detailed analyses of the axially and temporally resolved L-shell

spectra and a discussion of the implications of the high-energy spectrum. An analysis of the radially resolved L-shell spectra will be presented in a future paper.

1. High-energy spectra

High-energy emission from the Mo plasma was measured by a spectrometer using a convex LiF crystal having a 25.4 mm radius. The x-rays were collected on Kodak 2497 film. Because the high-energy emission was expected to be weaker than the abundant L-shell x-rays, no imaging slit was used on the beam-line, and therefore the high-energy spectra are integrated in both time and space. L-shell x-rays were filtered out of the incident beam with 0.1 mm of aluminum and 0.3 mm of polyamide. This combination of filters has 10% transmission at 7.2 keV.

The best measurements of high-energy spectra were obtained from the 55 mm array. Figure 3 shows Mo K_α and K_β emission features centered at 17.4 keV and 19.6 keV, respectively. The features are broad enough to encompass inner-shell emission from a wide range of charge states, from neutral Mo to the L-shell Mo ions. The energy emitted in the K_α and K_β lines was estimated using equations (3) and (11) of Ref. [24] to be 3 kJ -- about 4% of the L-shell yield and approximately 0.2% of the total radiated energy.

2. Axially resolved spectra

Axially resolved spectra were collected using a mica crystal bent into a 25.4 mm radius. A 0.20 mm-wide imaging slit oriented perpendicular to the plasma axis provided an axial resolution of 0.6 mm. The collected emissions were filtered to exclude low-energy photons with 25.4 μm of Be, which has 10% transmission at 1.1 keV. By virtue of its large 2-D spacing (19.84 Å), the mica instrument captured a wide range of emission, including emission in 2^{nd} order. Time- and space-integrated spectra from the three Mo wire arrays are given in Fig. 4, on which the most intense Ne-like lines are labeled according to their ion species and the configurations of the transitioning electron. The

most prominent spectral features are the 3-2 Ne-like Mo lines and 3-2 emission features from Na-like and F-like Mo. [27]

The spectra in Fig. 4 were obtained by averaging the axially resolved spectra along the height of the image, which covers 12 mm of the cathode end of the emitting plasma (the remaining 8 mm of emitting plasma were occluded by anode hardware). The axially resolved film image of the L-shell emission from the 50 mm wire array is shown in Fig. 5. For each of the three experiments, the 12 mm image of the plasma column was divided into six sections of 2 mm each for spectroscopic analysis. Note that the emission from the cathode end of the measured plasma column is about twice as intense as the emission from the anode end.

3. Time-gated spectra

To measure the evolution of the plasma column before and after its stagnation on the axis, a time-gated mica crystal spectrometer with a micro-channel plate (MCP) detector was fielded. The detector used seven strips, each activated by a 2 ns-wide gate pulses with a 1 ns inter-strip gap. This timing gives a 20 ns window for the collection of first order L-shell emission. The camera was timed to capture emission near the peak intensity of the L-shell emission from the wire array plasmas.

Seven time-gated spectra from the 50 mm-diameter array are shown in Fig. 6 and labeled with times relative to the peak total radiated power (see Fig. 2). The time-gated spectra capture the L-shell emission from approximately 3 ns before the peak total power to 15 ns afterwards. The lower-energy ($h\nu < 2.2$ keV) continuum emission is intense during the early frames and diminishes with time, while the L-shell line emission intensities persist through the peak of the L-shell power pulse.

Because there is some uncertainty in the voltage amplitude applied to each individual strip of the MCP, quantitative comparisons of the absolute spectral intensity between frames can be misleading. For example, with the voltages used in these tests, a variation

of just 2% in the voltage amplitude could result in a 17% variation in gain. Furthermore, there is additional uncertainty in the timing of the MCP camera, on the order of 1 ns, relative to the emitted power pulse as measured by the filtered PCDs. For the spectroscopic analysis the spectrum from each MCP frame was scaled to the energy in the power pulse integrated over that frame's 2 ns duration. While there is some uncertainty in this energy, the spectroscopic diagnostics are based on relative line intensities (see below), therefore this scaling does not introduce additional uncertainty to the diagnostic analysis.

III. L-SHELL MO MODELS

The axially resolved and time-gated spectra from the three Mo wire array experiments have been analyzed with a collisional-radiative, non-LTE atomic kinetic model. The primary model used for diagnostics in this paper is based on a complete set of self-consistent data calculated using the HULLAC suite of atomic structure codes. [36] [37] More than 6000 levels in O-like through Mg-like Mo are modeled, including singly excited states with n up to 7 and doubly excited states with n up to 4 in Na- and Mg-like Mo. Ground states of all ions from the bare ion to the neutral atom are also included. The levels are coupled by collisional excitation, collisional ionization, radiative and dielectronic recombination, radiative decay, and the reverse rates of the collisional process through detailed balance. Selected energies and radiative decay rates in the Ne-like ion were calculated using [38]. This model has previously been applied to diagnose plasma conditions using 3-2 Mo spectra from X pinch plasmas generated on smaller devices, specifically at the University of Nevada, Reno's 1 MA Zebra device [27] and Cornell University's 470 kA XP pulser. [29]

A second, independent, model has been constructed and is used in this paper to demonstrate the reliability of the L-shell diagnostics. This model includes only ~ 2000 levels with $n \leq 5$ in O-like through Mg-like Mo and is based on a data set compiled from several sources: energy levels and most radiative decay rates were calculated using [39];

Auger decay rates and selected Ne-like energies and radiative decay rates were calculated using [38]; collisional excitation cross sections from low-lying states were taken or interpolated from [40 41 42]; and collisional ionization and radiative recombination cross sections were approximated using a modified Lotz [43] and Kramers [44] approximations, respectively. The primary differences between the two models are: 1) the number of modeled levels – the HULLAC model has significantly more, and 2) the coupling between excited levels – since the compiled model includes only electric dipole radiative decay rates among excited levels and approximates many collisional cross sections using the Van Regemorter formulation, the coupling among excited states is much more complete and accurate in the HULLAC model.

The energy levels and rates in each of these models form sets of coupled linear equations whose coefficients are dependent on the plasma conditions (the electron temperature T_e and electron density n_e). These equations are solved in the steady-state approximation (which is adequate for the ns-scale time resolution of the experimental data) to obtain populations of the modeled energy levels, from which modeled spectra and charge state balances can be calculated. The modeled spectra are constructed using line intensities proportional to upper level populations and radiative decay rates and line distributions given by Voigt profiles whose width and shape are varied to match the experimental data. Figure 7 shows the 3 - 2 and higher-Rydberg regions of the modeled L-shell Mo spectrum decomposed into contributions from individual charge states and identifies diagnostically important lines and features.

The Ne-like lines are of particular importance in determining the electron density. At low densities, the long-wavelength 3F and 3G lines (transitions from $2s^2 2p^5 3s\ ^1P_1$ and $2s^2 2p^5 3s\ ^3P_1$ to $2s^2 2p^6\ ^1S_0$) are populated in a large part by radiative cascades from more highly excited levels that cannot decay directly to the Ne-like ground state. As the electron density increases, electron-ion collisions disrupt the radiative cascades, causing the intensities of the 3F and 3G lines to substantially decrease. The ratio of the intensity sum of the 3A and 3B lines (transitions from $2s\,2p^6 3p\ ^1P_1$ and $2s\,2p^6 3p\ ^3P_1$, respectively, to $2s^2 2p^6\ ^1S_0$) to that of the 3F and 3G lines decreases monotonically with the electron

density, is fairly insensitive to the electron temperature, [27] and can be used to isolate the electron density to within about a factor of two. Once the electron density is determined, the electron temperature can be found with an accuracy better than 10% by fitting the modeled charge state balance to the experimental data using the F-like feature labeled F1 in Fig. 7 and the Ne-like 3A line. More details of the HULLAC model and diagnostic procedures are given in [27].

The error estimates given above for the temperature and density diagnostics are determined in part by the precision of the diagnostic ratios that are extracted from the experimental data and in part by the reliability and accuracy of the diagnostic model. (By contrast, the precision of the diagnostics using a single model is limited only by the precision of the experimental data, so the trends in the spectroscopic data noted below are determined with fairly high confidence.) Figure 8 shows a comparison of spectra constructed using the two models detailed above; the good agreement between the independent models supports the accuracy and reliability of the L-shell diagnostics used here.

IV. SPECTROSCOPIC ANALYSIS

Spectra representing the emission of the wire array plasma averaged over space and time were obtained by integrating the axially resolved measurements for each of the three wire array plasmas (see Fig. 4) and were diagnosed using the model described above. The low-level background radiation evident in the spectra given in Fig. 4 was fit to a continuum curve and subtracted before the L-shell line analysis was performed. For all three arrays, the continuum temperature giving the best fit to the slope of the background emission was around 300 eV. Figure 9 shows a comparison of the integrated experimental and best-fit modeled spectra for the 50 mm-diameter array. The procedure described above of fitting line ratios gives T_e = 1.55 keV and n_e = 2 x10^{21}cm^{-3}. The modeled spectral lines and features in both the 3 - 2 and the higher-Rydberg spectral regions match the experimental features very well, even though many of those spectral features were not

constrained to fit the experimental data and the modeled higher-Rydberg spectral region has not been renormalized to fit the experimental intensities. The single point of significant disagreement is near 3.45 Å in the high-Rydberg region, where Na-like 5-2 satellites that are not included in the HULLAC data set are present in the experimental spectrum.

The fit quality of the integrated spectrum from the 50 mm-diameter wire array shown in Fig. 9 is representative of the entire experimental series. The integrated spectra from the two other arrays are diagnosed to have very similar plasma conditions: the 45 and 55 mm-diameter arrays have temperatures of 1.55 and 1.60 keV and densities of 2.1 and 1.8 x 10^{21}cm^{-3}, respectively. Estimates of the fraction of the initial wire array mass that radiates in the L-shell can be obtained using the diagnosed average plasma conditions. Radiative loss rates calculated with the spectroscopic model can be used to determine the number of L-shell ions required to produce the L-shell yields given in Table 3. For each of the three wire arrays, the necessary number of L-shell ions is 1-3x10^{18}, giving radiating mass fractions of 14%, 13%, and 8% for the 45, 50, and 55 mm arrays, respectively. The number of ions required to produce the measured L-shell emission is also very close to the number of ions that would be present in a 20 mm plasma column at the diagnosed plasma conditions with a diameter of 1-2 mm (as indicated by the pinhole images given in Fig. 1 (b)).

A. Axially resolved spectra

Six axially resolved, time-integrated spectra from the 50 mm-diameter array are shown in Fig. 10 along with the best-fit modeled spectra and the diagnosed plasma conditions. The six spectra, taken in 2 mm increments from the observed 12 mm of the plasma column, are diagnosed to have electron temperatures that vary slightly from 1.55 to 1.65 keV from the anode end of the plasma to the cathode and densities that vary significantly from 3.0 to 0.8 x10^{21}cm^{-3} from the anode end to the cathode. These conditions bracket the diagnosed conditions of the associated time-integrated spectra. The axial dependence of temperature and density in the 50 and 55 mm wire array plasmas are shown together in

Fig. 11. Both plasmas indicate a rough trend of decreasing densities and slightly increasing temperatures from the anode end of the plasma to the cathode.

The pinhole images of the 50 mm array given in Fig. 1 indicate that the anode end of the plasma column converges earlier and to a smaller radius than the cathode end, which is consistent with the diagnosed axial trend of increasing electron density from the cathode to the anode, since better convergence should correspond to higher densities. Both the pinhole images and the higher time-integrated L-shell intensity observed at the cathode indicate that the anode-end plasma goes dark before the cathode. These measurements are consistent with an imploding plasma column that first converges to fairly high densities near the anode and has somewhat poorer and later convergence near the cathode, where it radiates at a lower density from a relatively large plasma region over a relatively long time – possibly maintained by trailing mass from the implosion flowing into the radiating plasma near the cathode.

B. Time-gated spectra

As shown by the plots of the L-shell and total radiated power given against time in Fig. 2, the L-shell radiation from each of the three arrays begins about 100 ns after the onset of the current pulse and peaks (at least for the 45 and 50 mm-diameter arrays) about 3 ns after the peak of the total radiated power. The L-shell radiation lasts for 20 – 30 ns and is broadly characterized by a 10 – 20 ns burst of intense x-rays that include significant low-energy continuum intensity followed by a 10 – 20 ns tail of lower-intensity radiation consisting mostly of L-shell line radiation (see Fig. 6).

Figure 12 shows six of the time-gated spectra from the 50 mm-diameter array, along with the best-fit modeled spectra and the diagnosed plasma temperatures and densities. The variation in plasma parameters is greater with time than with either the axial dimension or among the three initial wire diameters: the electron temperature varies from 1.55 to 1.80 keV and the electron density varies from 0.3 to 3.0 $x10^{21}cm^{-3}$, with the highest density and lowest temperature diagnosed at the onset of the L-shell radiation pulse. The

spectrum from the first MCP frame (see in Fig. 6) could not be fit well by the optically thin model, but appears to confirm the trends established by the better-fit, subsequent data showing decreasing density and increasing electron temperature with time. (The difficulty in fitting this frame's data may be overcome by including opacity effects in the analysis: this topic will be addressed in a future paper.)

The plasma parameters diagnosed from the time-gated spectra from the 50 and 55 mm wire arrays are given together in Fig. 13. The trends of decreasing density and increasing temperature with time are apparent in both arrays, with the 55 mm array having the least variation in time. This may be understandable in relation to the measured L-shell power from that array, which had three distinct peaks and radiated for a longer time with a smaller intensity than the other two arrays (see Fig. 2), suggesting more complex implosion dynamics. Finally, note that the plasma conditions diagnosed from the late-time emission of the arrays are close to those diagnosed from the cathode emission, a congruence consistent with the plasma dynamics suggested above.

C. High-energy spectra

The high-energy spectrometer recorded approximately 3 kJ of energy emitted in 17 - 20 keV inner-shell K_α and K_β Mo transitions. Although the present models do not include excited states formed by excitation of an inner-shell (1*s*) electron, rough estimates of the energy emitted in the K_α lines from Ne-like Mo ions have been obtained using data calculated with the atomic structure code FAC. [45] For a plasma dominated by Ne-like ions at the average diagnosed plasma conditions, less than 10 J of K-shell Mo photons would be emitted over 15 ns from a uniform column 12 mm in length and 1 mm in diameter. Since only a few percent of the Mo atoms present in the initial wire array must reach near Ne-like ions in order to account for the measured L-shell yields, and on the assumption that inner-shell emission rates are similar for most charge states of Mo, up to several hundred Joules of energy may be emitted in K-shell lines if all the Mo atoms present in the initial wire array participate in the K_α and K_β radiation. However, this is still much less than the observed 3 kJ of K-shell emission, suggesting that the electron

energy distribution in the wire array plasma is not purely Maxwellian and includes a fraction of electrons with energies greater than about 20 keV. By a rough estimate, the observed energy in the K_α and K_β lines can be accounted for by including a fraction between 0.1% and 1% of such high-energy electrons, which could be accelerated by the strong electric fields present in the diode.

High-energy electrons with energies of several or tens of keV can affect L-shell as well as high-energy inner-shell emission spectra. [27] Their primary effects on L-shell spectra include increasing the intensities of Ne-like Mo lines that are fed in part by radiative cascades (3A, 3B, 3F, and 3G), changing the structure of satellite emission features, and spreading out the charge state balances. [46] The first effect would indeed improve the fit of the modeled spectra to the experimental data, particularly for those spectra diagnosed to have densities above about 10^{21} cm^{-3}. However, a similar effect can be caused by self-absorption of the Ne-like Mo 3C and 3D lines and can be difficult to deconvolve from the effects of high-energy electrons. Further, the diagnosed bulk temperatures are so large that the effects of small fractions of high-energy electrons on L-shell rates and ion abundances are washed out by thermal electrons with energies above ~ 5 keV, and the detailed structure of the satellite features is obscured by broad spectral lines. The L-shell spectra are therefore consistent with the existence of a small fraction of high-energy electrons but do not offer an unambiguous confirmation of their presence. Spectropolarimetry or other measurements will be needed to confirm the presence of and quantify the amount of non-thermal electrons.

V. DISCUSSION

A major observation of this work is the presence of the long wavelength axial gradient shown in Figure 11. Long wavelength variations in x-ray emission are well known in gas puff Z-pinch plasmas, where axial variations in the flow characteristics of the gas nozzles result in zippering [8 47], that is, a time dependent stagnation on the axis. Experiments with tilted nozzles [48] demonstrated that this effect could be minimized. However, since wire arrays have a uniform mass per unit length and are axially very well aligned in a right

cylinder, it is somewhat unexpected that a long wavelength structure would be so prominent. Short wavelength (< 0.5 mm) axial structures are observed in the wire arrays as they ablate at their original radial location [49] [50] and few millimeter wavelengths are observed in the imploding plasma structure [51]. Regarding the observed long wavelength structure, one hypothesis may be that since we only observe one electrode we are actually observing edge effects cause by the electrodes. Magneto-hydrodynamic (MHD) simulations predict that these can occur. Another hypothesis is that there is an axial zippering in wire arrays. Some data [Fig. 4 in Ref. 51] have indicated that the initiation of the wires can vary along the axial length starting near the cathode. To resolve which is the correct hypothesis will require diagnostics that can image both electrodes. In either model, the observed gradients could be having an impact on radiation symmetry in ICF concepts such as the dynamic hohlraum [52] [53].

These experiments also provide the first data on kilovolt L-shell x-ray emissions from a Z-pinch plasma with Z>22 on a greater than 10 MA accelerator, and as such, they provide an opportunity to understand some of the scaling issues associated with moving to higher atomic number K-shell radiators. This is especially true since the space- and time-resolved spectra have enabled an analysis of the imploded plasma conditions.

A few observations can be made from the spectral data. Firstly, a sizable amount of mass (> 100 μg/cm) was ionized into the L-shell; however, this represents only a small fraction of the initial mass (10%). This mass was ionized into the lower stages of the L-shell (30% neon-like and 30% fluorine-like) due to the low electron temperature, 1.5 to 1.7 keV. Secondly, the remainder of the mass has an electron temperature no more than 300 eV, as determined from the free-bound slope into the M-shell. The intensity of this slope suggests that this portion of the plasma has significant opacity, and therefore could represent a significant fraction of the mass. Could the 10% L-shell mass fraction and lower ionization level be due to the implosion dynamics of the molybdenum arrays?

If we assume that high atomic number plasmas on Z have the ability to radiate at about the rate the plasma is being heated, the maximum radiated power therefore becomes a

good indicator of the maximum heating rate. The measured total radiated powers of 150 TW (for the 45 and 50 mm arrays) suggest an efficient heating rate. In fact, 150 TW is consistent with implosions at around 80 cm/μs and radial mass distribution scale lengths of a few millimeters. A few millimeter scale length is consistent with the final plasma diameters (2-3 mm) as measured by the time-resolved pinhole cameras, and the measured peak electron densities are also consistent with a few millimeter diameter plasma. None of these considerations indicate poor implosion quality as the major issue causing the lower efficiency of ionization of the molybdenum into the L-shell. It should be noted that locally the fraction of mass ionized into the L-shell could be higher. The axially resolved spectra indicate significant variation in implosion conditions along the axis with a definite trend towards less compression (lower density) near the cathode. The observed axial gradient could account for a 50% improvement in L-shell emission if the L-shell yield per unit length of the anode region could be reproduced over the entire length, but the temperatures and ionization balances are not too different at the different axial locations. Even at the best conditions in the stagnated plasma the ionization is still in the lower L-shell stages. The obvious conclusion is that it will be difficult to heat these higher Z materials to the K-shell if we can only achieve minimal ionization into the L-shell.

As we discussed in the introduction, Mulbrandon *et al*. [32] have shown the details of the radiation losses from lower ionization states of high atomic number elements can result in clamping of the electron temperatures. It is also well known that unless the plasma is being heated significantly, it is likely that plasmas will end up in a closed shell configuration (i.e. helium-like or neon-like) due to the large disparity between the ionization energy to get into the ground state of the closed shell configuration versus the ionization energies of the next higher ionization stages.

These molybdenum experiments could enable direct comparison of calculations with experiments, but at the moment, there are no two- or three-dimensional MHD codes with detailed radiation transport for molybdenum. However, some information can be deduced from comparing the molybdenum results to data from other lower atomic

number plasma implosions on Z. Table 4 summarizes the comparison of argon, titanium, and molybdenum implosions on Z. Clearly, the molybdenum implosions has similar energy coupling, i.e. the total radiated yields were similar. Comparing the argon data from a nested shell implosion, to the titanium data from a low wire number nested array, indicates that the argon implosion produced similar temperatures but had a much higher density. This fact coupled with the lower photon energy of the argon K-shell emissions (3.3 keV vs 4.8 keV) resulted in two and half times more K-shell yield than in titanium. The molybdenum implosions have high electron densities as well, very comparable to the argon data, but the electron temperatures were only 1.5 to 1.7 keV. This is probably indicative of the molybdenum being a more copious radiator, that is, more energy is lost as the Mo ionizes through ~ 32 stages than is lost by the lower-Z materials as they ionize over ~ 20 stages, and M-shell emission channels in Mo contribute more to radiation losses than L-shell channels in Ti or Ar. Indeed, the optically thin radiative cooling rates per ion given by Post [47] are ~ 30 times larger for Mo at 1.6 keV than for either Ti at 3.0 keV or Ar at 2.2 keV. Because the Mo plasma reaches a higher density than the Ti plasma, its radiative cooling rate may be more than 100 times greater. Also, as the plasma's average opacity increases the electron temperature and the radiation temperature will become closer, or in other words, the emitted radiation will begin to limit the peak electron temperatures achieved for a given heating rate.

Detailed radiation-MHD calculations will be needed so that these phenomena can be studied in detail. Included in these studies, MHD calculations can be used to assess the distribution of η values achieved in implosions compared to the average η calculated from zero-dimensional simulations. Douglas *et al*. [55] has shown in 2-D calculations that the peak velocity achieved is usually less than that determined from a 0-D calculation. For wire arrays, Lebedev *et al*. [56] has shown that very non-0-D like trajectories are common, and that some parts of the plasma may achieve velocities higher than the 0-D value, whereas some parts achieve velocities less than the 0-D value. All of these can affect the heating rate in the stagnated plasma. Considering all these complexities we can conclude that based on the L-shell ionization levels, wire array implosions that intend to

ionize molybdenum into the K-shell will need to obtain η values very much higher than the typical $2<\eta<5$ to obtain optimum K-shell yields from materials with $Z<22$.

VI. SUMMARY AND FUTURE WORK

In summary, we have measured the stagnated plasma conditions of molybdenum arrays on the 20-MA Z accelerator by performing spectroscopic analyses of the dominant L-shell emissions. The measured electron temperatures were in the range of 1.5 to 1.7 keV, and they had little variation either along the axial direction of the Z-pinch nor in time during the stagnation. Peak electron densities of $3 \times 10^{21} cm^{-3}$ were measured and the axially resolved spectra indicated variations from this value of a factor of five or more along the z-axis. Time-resolved spectra indicate the electron densities peaked at the onset of L-shell emissions and then decreased during the radiation pulse. Estimates suggest at peak some 10% of the initial mass was heated into the L-shell.

Although the L-shell emissions were thermal in origin, the spectra may have shown some influence of electron beams or finite opacity. Clearly, low current e-beams were present as evidenced by the observation of characteristic inner-shell emissions; however, being time-integrated emissions we cannot state when the beams occurred. Future analysis of the radially resolved L-shell spectra will enable us to estimate the role of opacity in the L-shell emissions.

Future calculations will involve the use of detailed radiation-MHD calculations to compare to the measured L-shell spectra along with the other radiation characteristics of the stagnated plasmas. Future experiments will probably wait for the arrival of the upgrade to Z [57]. The higher current available on ZR will enable implosions with similar or even higher masses than in the experiments reported in this paper from larger diameters. The higher heating rates available on ZR may also result in greater ionization levels. These future experiments will include simultaneous measurements of spectra in time and space.

ACKNOWLEDGEMENTS

The authors would like to acknowledge the valuable assistance of D.S. Nielsen, T.C. Moore, and D.O. Jobe for fielding the spectrometers on the Z accelerator and J.E. Bailey and P.W. Lake for their guidance in spectrometer design, operation, and data analysis. The authors thank J.F. Seamen, R.J. Leeper, R.S. Spielman, M.A. Hedemann, D.H. McDaniel, M.K. Matzen, and J.P. Quintenz for sustained programmatic support. Sandia is a multiprogram laboratory operated by Sandia Corporation, a Lockheed Martin Company, for the United States Department of Energy under contract No. DE-AC04-94AL85000. The work of S.H. and A.S. was supported in part by Sandia National Laboratories under contract 27625. The work of K.F. (and S.H. in part) was performed under the auspices of the U.S. Department of Energy by University of California Lawrence Livermore National Laboratory under contract No. W-7405-Eng-48.

REFERENCES

[1] N. R. Pereira and J. Davis, J. Appl. Phys. **64**, R1 (1998).
[2] C. Deeney, P. D. LePell, F. I. Cochran, M. C. Coulter, K. J. Whitney, and J. Davis, Phys. Fluids **5**, 992 (1993).
[3] C. Deeney, P. D. LePell, and B. H. Failor, *et al*., Phys. Rev. E **51**, 4823 (1995).
[4] K. G. Whitney, J. W. Thornhill, and J. L. Giuliani Jr, *et al*., Phys. Rev. E **50**, 2166 (1994).
[5] C. Deeney, T. J. Nash, and R. B. Spielman *et al*., Phys. Plasmas **5**, 3431 (1998).
[6] H. M. Sze, J. S. Levine, and J. W. Bannister *et al*., IEEE-Transactions on Plasma Science **30**, 532 (2002).
[7] C. Deeney, C. A. Coverdale, and M. H. Douglas *et al*., Phys. Plasmas **6**, 2081 (1999).
[8] H. Sze, P. L. Coleman, and J. Banister *et al*., Phys. Plasmas **8**, 3135 (2001).
[9] K. G. Whitney, J. W. Thornbill, J. P. Apruzese, J. Davis, and J. Appl. Phys. **67**, 1725 (1990).
[10] J. W. Thornbill, K. G. Whitney, C. Deeney, and P. D. LePell, Phys. Plasmas **1**, 321 (1994).
[11] T. W. Hussey, N. F. Roderick, U. Shumlak, R. B. Spielman, and C. Deeney, Phys. Plasmas **2**, 2055 (1995).
[12] D. I. Peterson, R. I. Bowers, K. D. McLenithan, C. Deeney, G. A. Chandler , R. B. Spielman, M. K. Matzen, and N. F. Roderick, Phys. Plasmas **5**, 3302 (1998).
[13] K. G. Whitney, J. W. Thornhill, J. P. Apruzese, J. Davis, C. Deeney, P. D. LePell, and B. H. Failor, Phys. Plasmas **2**, 2590 (1995).

[14] S. V. Lebedev, R. Aliaga-Rossel, S. N. Bland, J. P. Chittenden, A. E. Dangor, M. Haines, and M. Zakaullah, Phys. Rev. Lett. **84**, 1708 (2000).
[15] F. I. Cochran, J. Davis, and A. L. Velikovich, Phys. Plasmas **2**, 2765 (1995).
[16] C. Deeney, M. R. Douglas, R. B. Spielman, T. J. Nash, D. L. Peterson, P. L'Eplattenier, G. A. Ch,ler, J. F. Seamen, and K. W. Struve, Phys. Rev. Lett. **81**, 4883 (1998).
[17] J. Davis, N. A. Gonderenko, and A. L. Velikovich, Appl. Phys. Lett. **70**, 170(1997).
[18] J. P. Apruzese P. E. Pulsifer, J. Davis, R. W. Clark, and K. G. Whitney *et al*., Phys. Plasmas **5**, 4476 (1998).
[19] J. P. Apruzese, Naval Research Laboratory Memorandum Report No 6720-99-8341, pp. 4-6 (1999).
[20] C. Deeney, T Nash, P. D. Lepell, K. Childers, M. Krishnan, K. G. Whitney, and J. W. Thornhill, J. Quant. Spectr. Radiat. Transf. **44**, 457 (1990).
[21] J. S. Levine, B. H. Failor, H. M. Sze, and D. Bell, IEEE-Transactions on Plasma Science **30**, 512 (2002).
[22] H. Gordon, M. G. Hobby, N. J. Peacock, and R. D. Cowan, J. Phys. B **12**, 881 (1979).
[23] V. A. Boiko, S. A. Pikuz, A. S. Safronova, and A. Y. Faenov, J. Phys. B **11**, L503 (1978).
[24] B. I. Henke, H. T. Yamada, and T. J. Tanaka, Rev. Sci. Instr. **54**, 1311 (1983).
[25] G. A. Chandler, C. Deeney, and M. Cuneo *et al*., Rev. Sci. Instr. **70**, 561 (1990).
[26] R. B. Spielman, Rev. Sci. Instr. **66**, 867 (1995).
[27] A. S. Shlyaptseva, S. B. Hansen, V. L. Kantsyrev, D. A. Fedin, N. Ouart, K. B. Fournier, and U. I. Safronova, Phys. Rev. E **67**, 26409 (2003).
[28] D. B. Sinars, S. A. Pikuz, T. A. Shelkovenko, K. M. Chandler, and D. A. Hammer, Rev. Sci. Instr. **72**, 2948 (2001).
[29] S.B. Hansen, A.S. Shlyaptseva, S.A. Pikuz, D.B. Sinars, T.A. Shelkovenko, K.M. Chandler, and D.A. Hammer (submitted to PRE).
[30] S. B. Hansen, A. S. Shlyaptseva, V. L. Kantsyrev, D. A. Fedin, N. D. Ouart, U. I. Safronova, and K. B. Fournier, Rev. Sci. Instr. **74**, 1943 (2003).
[31] B. J. MacGowan, M. D. Rosen, and M. J. Eckart *et al*., J. Appl. Phys. **61**, 5243 (1987).
[32] J. Davis, J. L. Giuliani, and M. Mulbrandon, Phys. Plasmas **2**, 1766 (1995).
[33] R. B. Spielman, C. Deeney, and G. A Chandler *et al*., Phys. Plasmas **5**, 2105 (1998).
[34] C. Deeney, M. R. Douglas, R. B. Spielman, T. J. Nash, D. L. Peterson, P. L'Eplattenier, G. A. Chandler, J. F. Seamen, and K. W. Struve, Phys. Rev. Lett. **81**, 4883 (1998).
[35] C. Deeney, J. P. Apruzese, and C. A. Coverdale, 2003, (submitted to Phys. Rev. Lett.)
[36] M. Klapish, J.L. Shwob, B.S. Fraenkel, and J. Oreg, J. Opt. Soc. Am. **67**, 148 (1977).
[37] A. Bar-Shalom, M. Klapisch, and J. Oreg, Phys. Rev. A **38**, 1773 (1988).
[38] U.I. Safronova, C. Namba, I. Murakami, W.R. Johnson, and M.S. Safronova, Phys. Rev. A **64**, 012507 (2001).
[39] R. D. Cowan, The Theory of Atomic Structure and Spectra (University of California Press, Berkeley, 1981).
[40] D.H. Sampson, H.L. Zhang, and C.J. Fontes, At. Data Nucl. Data Tables **48**, 25 (1991).

[41] H.L. Zhang, D.H. Sampson, R.E. Clark, and J.B. Mann, At. Data Nucl. Data Tables **37**, 17 (1987).
[42] H.L. Zhang, D.H. Sampson, R.E. Clark, and J.B. Mann, At. Data Nucl. Data Tables **41**, 1 (1989).
[43] H.A. Kramers, Philos. Mag. **46**, 836 (1923).
[44] V.A. Bernshtam, Y.V. Ralchenko, and Y. Maron, J. Phys. B **33**, 5025 (2000).
[45] M. F. Gu, Astrophys. J. **582**, 1241 (2003).
[46] S. B. Hansen, Ph.D. dissertation, University of Nevada, Reno (2003).
[47] T. W. Hussey, M. K. Matzen, and N. F. Roderick, J. Appl. Phys., **59** 2677 (1986).
[48] C. Deeney, P. D. LePell, F. L. Cochran, M. C. Coulter, K. G. Whitney, and J. Davis Phys. Fluids B **5**, 992 (1993).
[49] S. V. Lebedev, F. N. Beg, S. N. Bland, J. P. Chittenden, A. E. Dangor, M. G. Haines, K. H. Kwek, S. A. Pikuz, and T. A. Shelkovenko, Phys. Plasmas **8**, 3734 (2001).
[50] V. V. Alexandrov, E. V. Grabovsky, G. G. Zukakishvili, *et al*., JETP **97**, 745 (2003).
[51] S. V. Lebedev, I. H. Mitchell, R. Aliaga-Rossel, S. N. Bland, J. P. Chittenden, A. E. Dangor, and M. G. Haines, Phys. Rev. Lett. **81**, 4152 (1998).
[52] J. E. Bailey, G. A. Chandler, and S. A. Slutz *et al*., Phys. Rev. Lett. **92,** 085002 (2004).
[53] T. W. L. Sanford, R. C. Mock, and R. J. Leeper *et al*., Phys. Plasmas **10**, 1187 (2003).
[54] D. E. Post, R. V. Jensen, C. B. Tartar, W. H. Grasberger, and W. A. Lokke, At. Data Nucl. Data Tables **20**, 397 (1977).
[55] M. R. Douglas, C. Deeney, and N. F. Roderick, Phys. of Plasmas **8**, 238 (2001).
[56] S. V. Lebedev, F. N. Beg, S. N. Bland, J. P. Chittenden, A. E. Dangor, and M. G. Haines, Phys. Plasmas **9**, 2293 (2002).
[57] D. H. McDaniel, M. G. Mazarakis, and D. E. Bliss *et al.*, AIP Conference Proceedings **651** (5th International Conference on Dense Z-Pinches; June 23-28, 2002; Albuquerque, New Mexico), p. 23 (2002).

X-ray energy (keV)	K-shell Z	L-shell Z	K-shell E_{min} (keV/ion)	L-shell E_{min} (keV/ion)
1.0	10	28	5	12
1.7	13	36	13	35
2.7	16	42	26	68
3.3	18	47	42	111
4.8	22	54	89	215
7.9	30	74	286	709

Table 1. A comparison between K- and L-shell radiators and the minimum kinetic energy required to reach appropriate ionization states. L-shell radiators require about 2.6 times more energy per ion than K-shell radiators.

Array diameter (mm)	Outer array mass (μg/cm)	Total mass (mg)	Interwire gap (mm)	0-D implosion time (ns)	0-D implosion velocity (cm/μs)	Kinetic energy (eV/ion)	η (KE/E_{min})	
							L-shell	K-shell
45	1107	3.32	1.86	99	82	337	5.0	0.4
50	932	2.80	2.46	99	91	423	6.2	0.5
55	757	2.27	3.32	99	100	500	7.4	0.6

Table 2. Summary of experimental load configurations and predicted 0-D implosion characteristics. The nested arrays were 20 mm in length and had inner arrays with diameters and masses ½ that of the outer arrays. The configurations were designed to exceed (by a factor of η) the energy required to generate L-shell x-rays

Outer diameter (mm)	Peak Load Current (MA)	Total yield (kJ)	Peak total power (TW)	Total rise-time (ns)	Total FWHM (ns)	L-shell yield (kJ)	Peak L-shell power (TW)	L-shell rise-time (ns)	L-shell FWHM (ns)
45	18.1	1660	140	5.1	6.6	67	9.1	4.0	4.5
50	18.0	1500	160	2.7	5.2	77	8.4	5.0	6.4
55	18.0	1160	79	4.7	8.5	68	3.0	1.9	14

Table 3. Summary of radiative properties of the Mo wire arrays. The total yield, peak total power, and peak L-shell power tend to decrease with increasing array diameters, while the L-shell yield is relatively constant.

Radiator	X-ray energy (keV)	E_{min} (keV/ion)	T_e (keV)	n_e (10^{20} cm^{-3})	X-ray yield (kJ)	X-ray risetime (ns)	Total output (MJ)
Ar[8]	3.3	42	2.0-2.4	10-25	250	5-7	1.5
Ti[7]	4.8	89	2.7-3.2	4-6	90	1-3	1.4
Mo	2.7	68	1.5-1.8	10-30	75	2-5	1.6

Table 4. Summary of plasma parameters and radiation output characteristics of K-shell Ar [8] and Ti [7] and L-shell Mo radiation sources on the Z accelerator. The Mo source has smaller x-ray yields than both Ar and Ti despite having relatively low-energy x-ray emission.

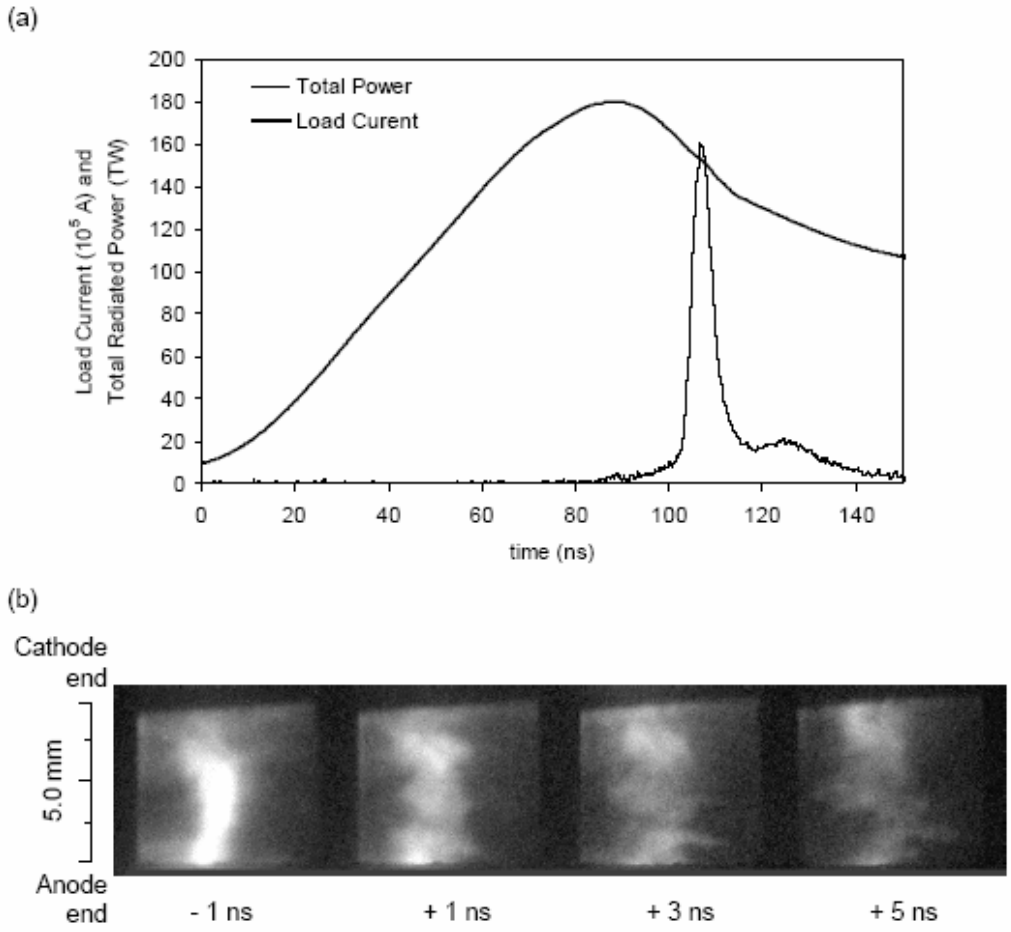

Fig. 1. (a) The measured load current and total radiated x-ray power for the 50 mm-diameter nested Mo array implosion. (b) Time sequences of pinhole camera images from the 50 mm-diameter implosions of the 50 mm-diameter Mo wire array on Z. Each image collected photons with energies > 1 keV over a 1 ns time-frame. The indicated times are relative to the peak total radiated power from each pinch. The images are from a 5.0 mm portion of the 20 mm plasma near the center. The small tilt evident in the images is due to the camera's slight misalignment.

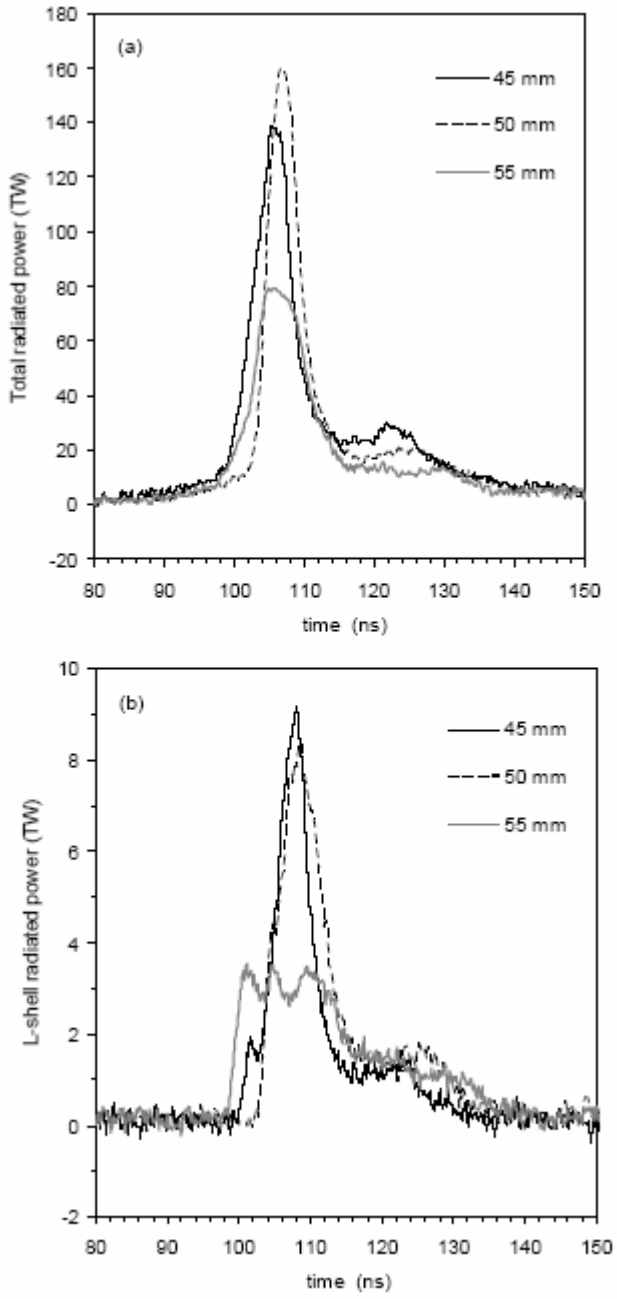

Fig. 2. (a) Total radiated power from three Mo wire arrays with the given initial diameters as measured by a filtered XRD. (b) L-shell (*hν* > 2.1 keV) radiated power from the arrays as measured by a filtered PCD. Times are given relative to the start

of the current pulse. The peak L-shell and total radiated powers of the 45 and 50 mm-diameter arrays are much larger than those of the 55 mm-diameter array.

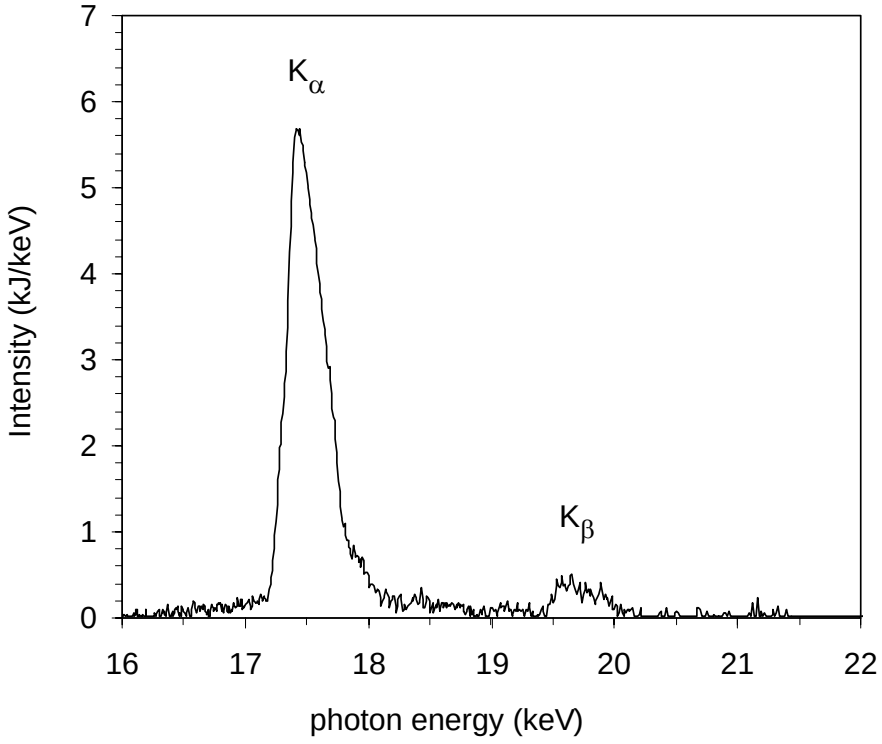

Fig. 3. Time- and space-integrated high-energy spectra from the 55 mm-diameter Mo array. The dominant feature consists of the K_α emission feature from Mo centered at 17.4 keV and is accompanied by the weaker K_β emission feature at 19.6 keV. The estimated energy in these inner-shell x-rays is 3 kJ.

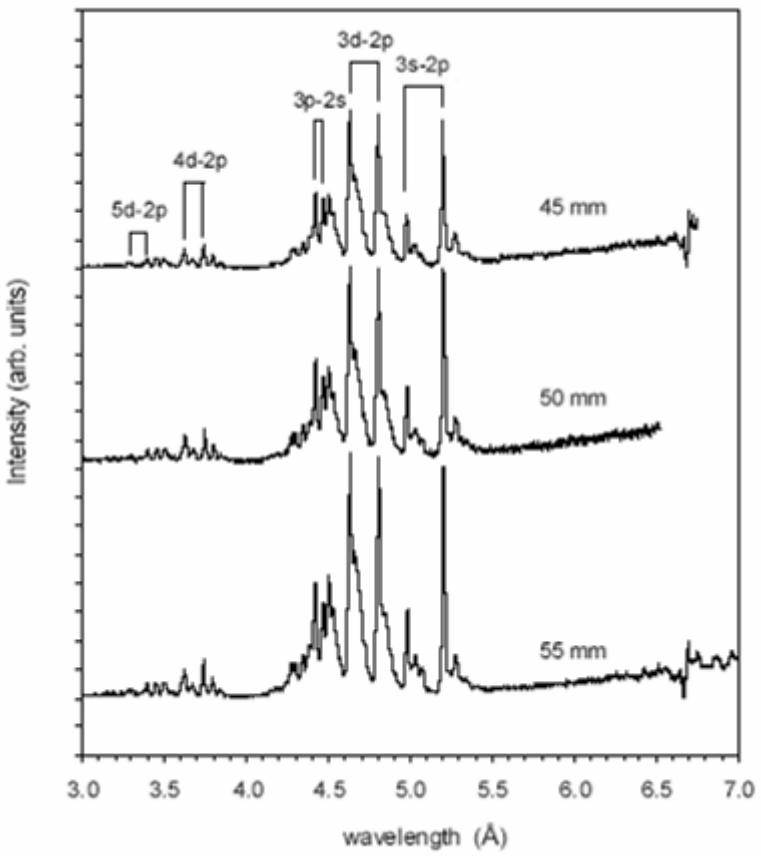

Fig. 4. First-order L-shell emission measured from the three Mo wire arrays. Selected Ne-like Mo lines are labeled with the initial and final *nl* of the associated radiative transition.

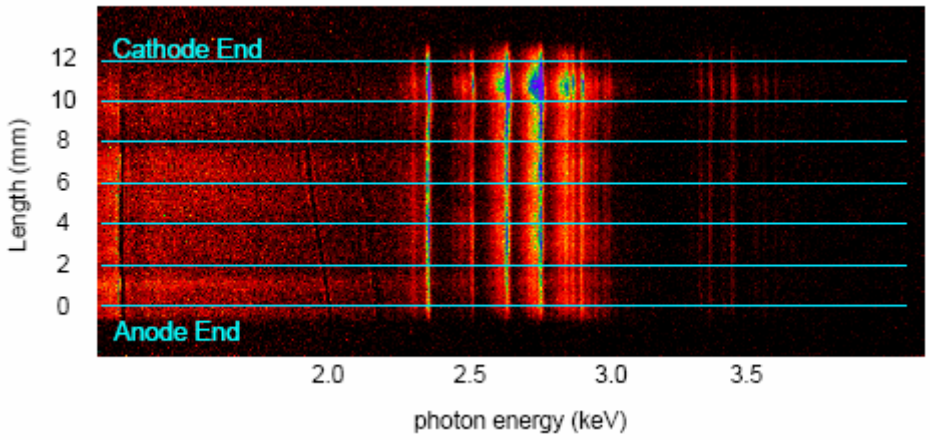

Fig. 5. Axially resolved film image from the 50 mm-diameter Mo wire array, representing 12 mm on the cathode side of the 20 mm plasma column. The image has axial resolution of 0.6 mm and was divided into six segments of 2 mm each for analysis. The cathode-end emission is twice as intense as the emission nearer the anode.

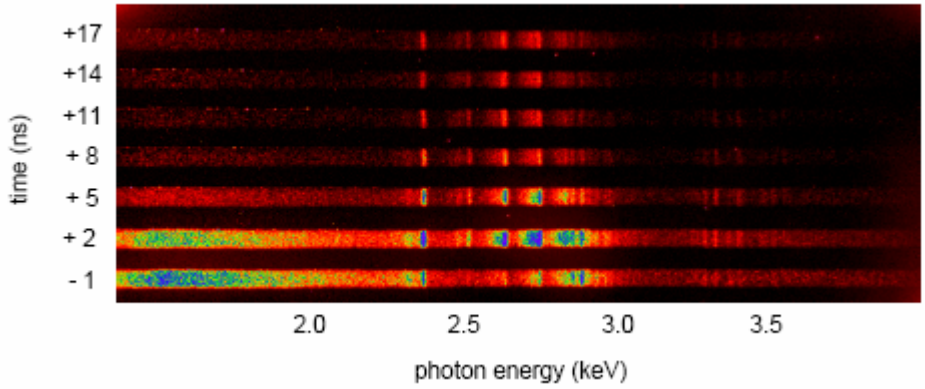

Fig. 6. Time-gated MCP spectra from the 50 mm-diameter array. The frame times run upward and are labeled with times relative to the peak total radiated power. The lower-energy continuum emission is quite intense in the early frames and

diminishes with time, while the line emission persists through the peak of the L-shell power pulse.

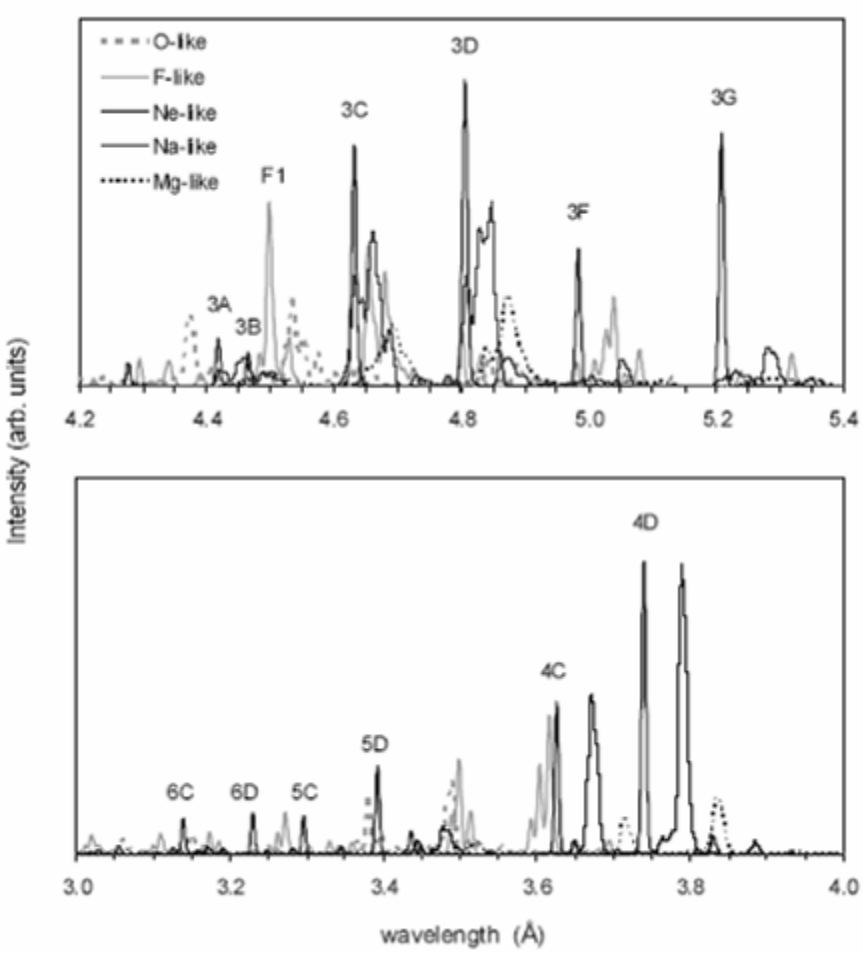

Fig. 7. L-shell Mo spectrum of 3-2 (a) and higher-Rydberg (b) lines and features decomposed into contributions from O- through Mg-like Mo. Most Ne-like lines and a diagnostically important F-like line are labeled.

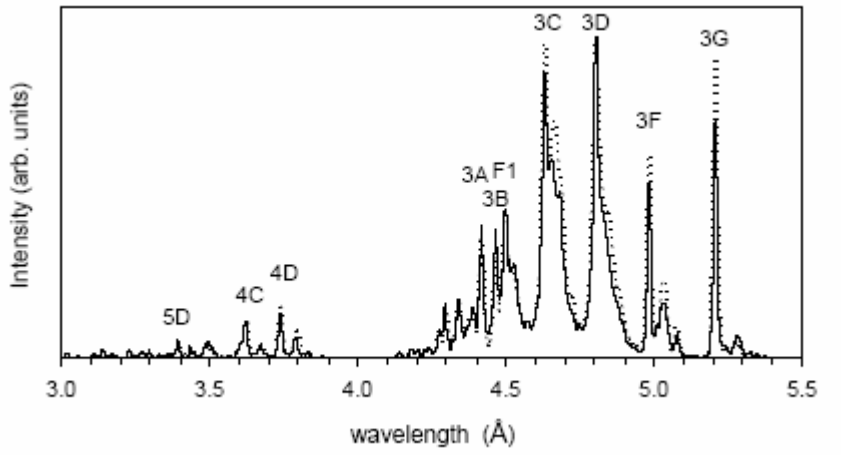

Fig. 8. Comparison of L-shell Mo spectra at T_e = 1.6 keV and n_e = 2 x 10^{21}cm^{-3} constructed using two models with different level structure and independent data sources. The good agreement between the HULLAC-based model (solid line) and the compiled model described in the text (dotted line) indicates that the L-shell diagnostics used here are reliable.

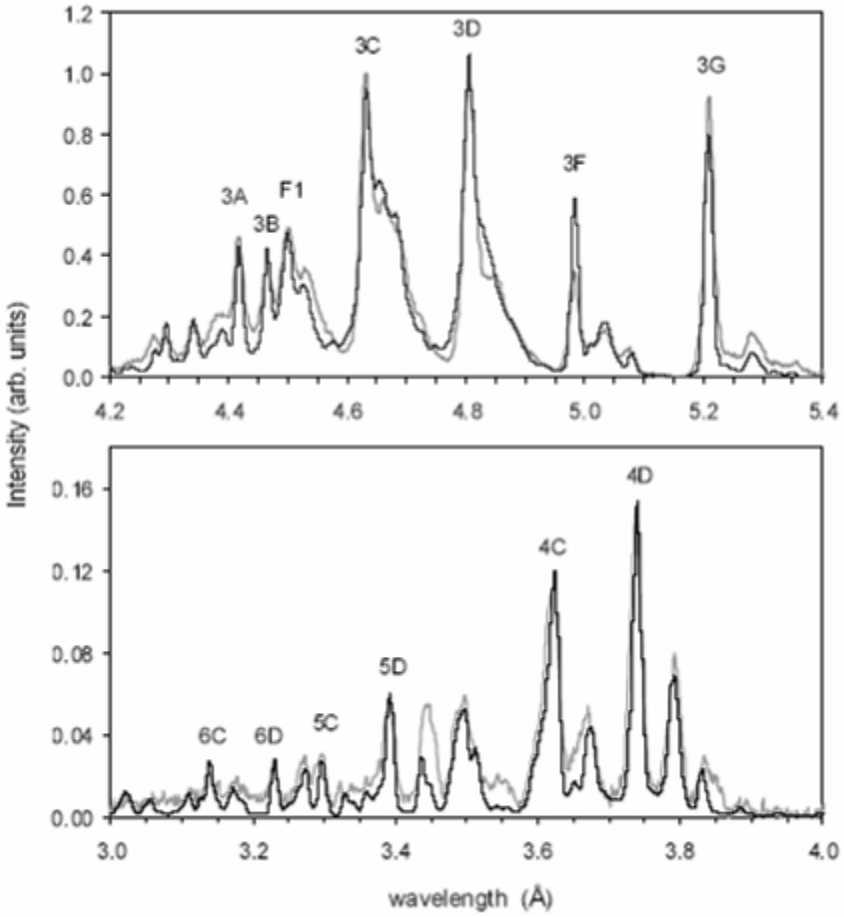

Fig. 9. Comparison of a modeled L-shell Mo spectrum at T_e = 1.6 keV and n_e = 1.8 x 10^{21}cm^{-3} with the space- and time-integrated spectrum from the 50 mm-diameter wire array plasma.

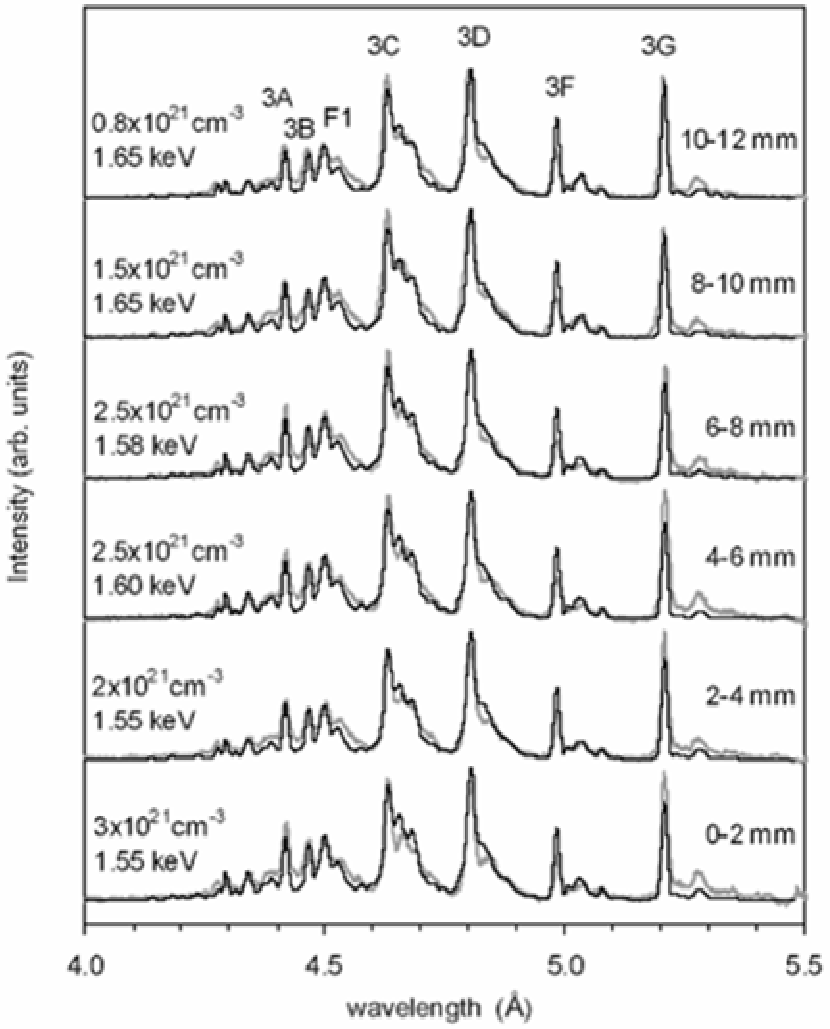

Fig. 10. Comparison of modeled L-shell spectra at the labeled conditions with six axially-resolved spectra from the 50 mm-diameter wire array plasma. The spectra, which are labeled according to their distance from the anode end of the axially-resolved plasma column, indicate increasing electron temperatures and decreasing electron densities from the anode to the cathode.

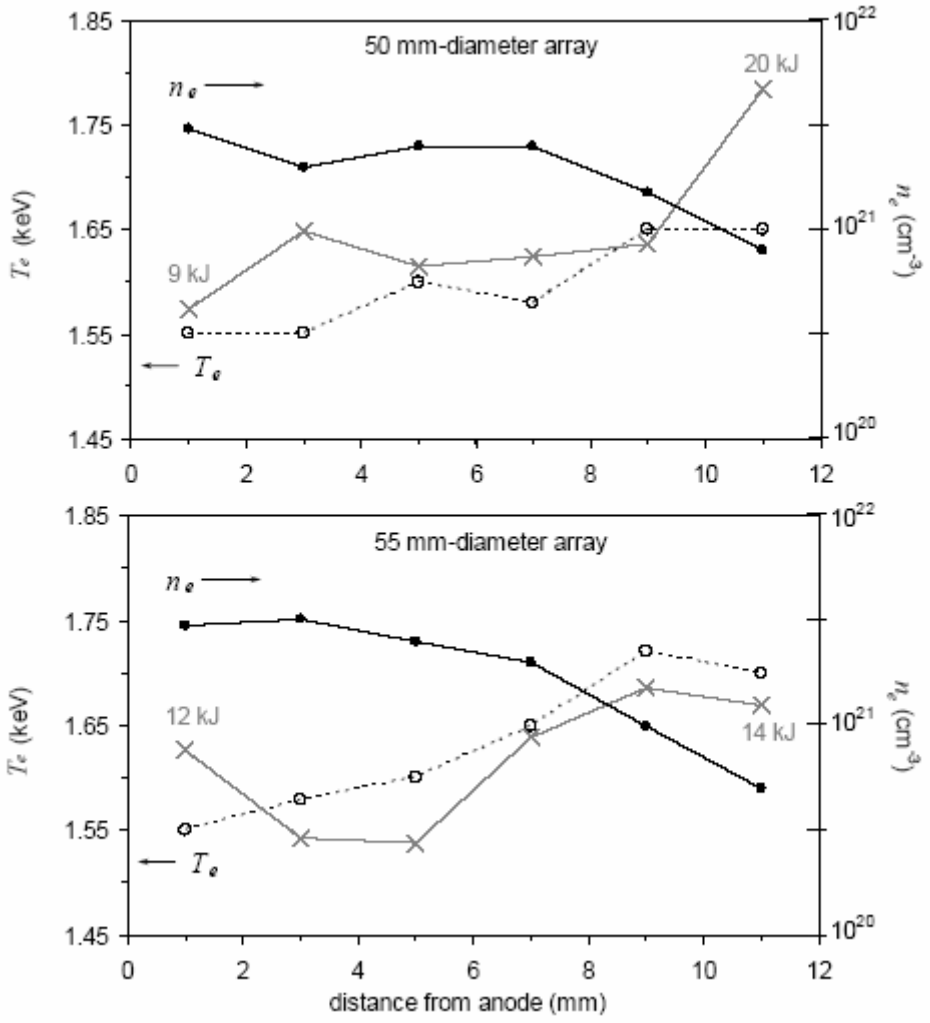

Fig. 11. Axial dependence of the diagnosed T_e and n_e from the 50 mm (black lines) and 55 mm (gray lines) wire arrays.

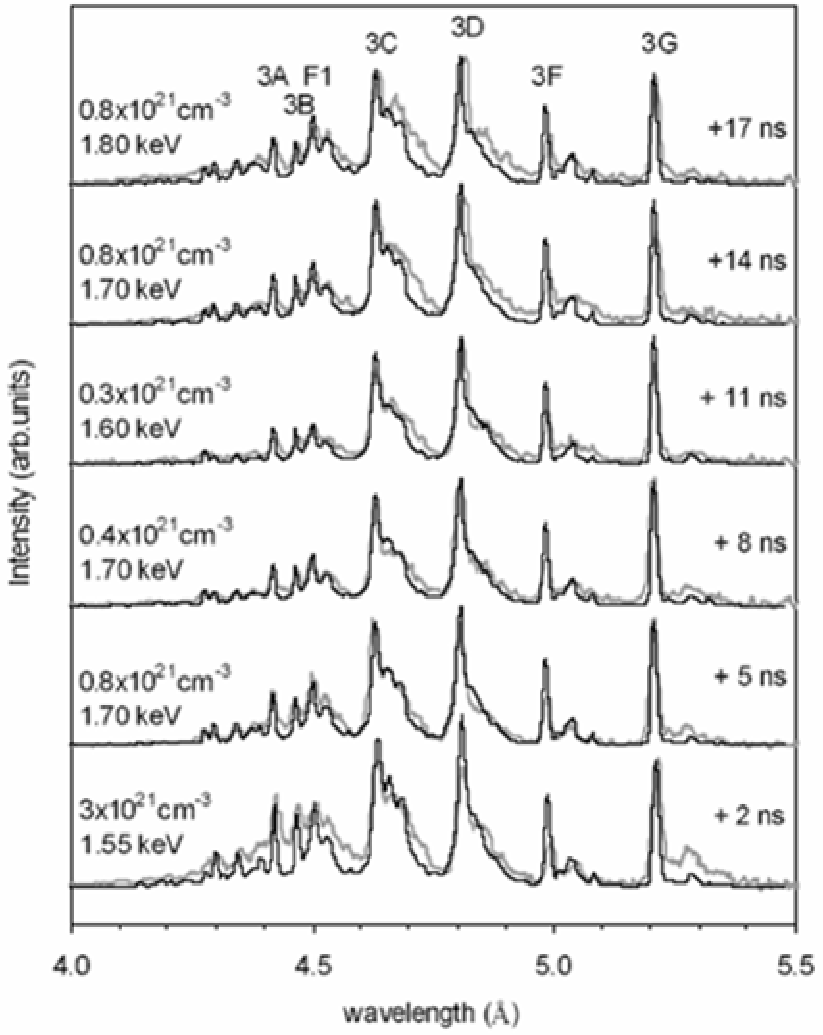

Fig. 12. Comparison of modeled L-shell spectra at the labeled conditions with six time-gated spectra from the 50 mm-diameter wire array plasma. The spectra are labeled with times relative to the peak total radiated power and indicate increasing electron temperatures and decreasing electron densities with time.

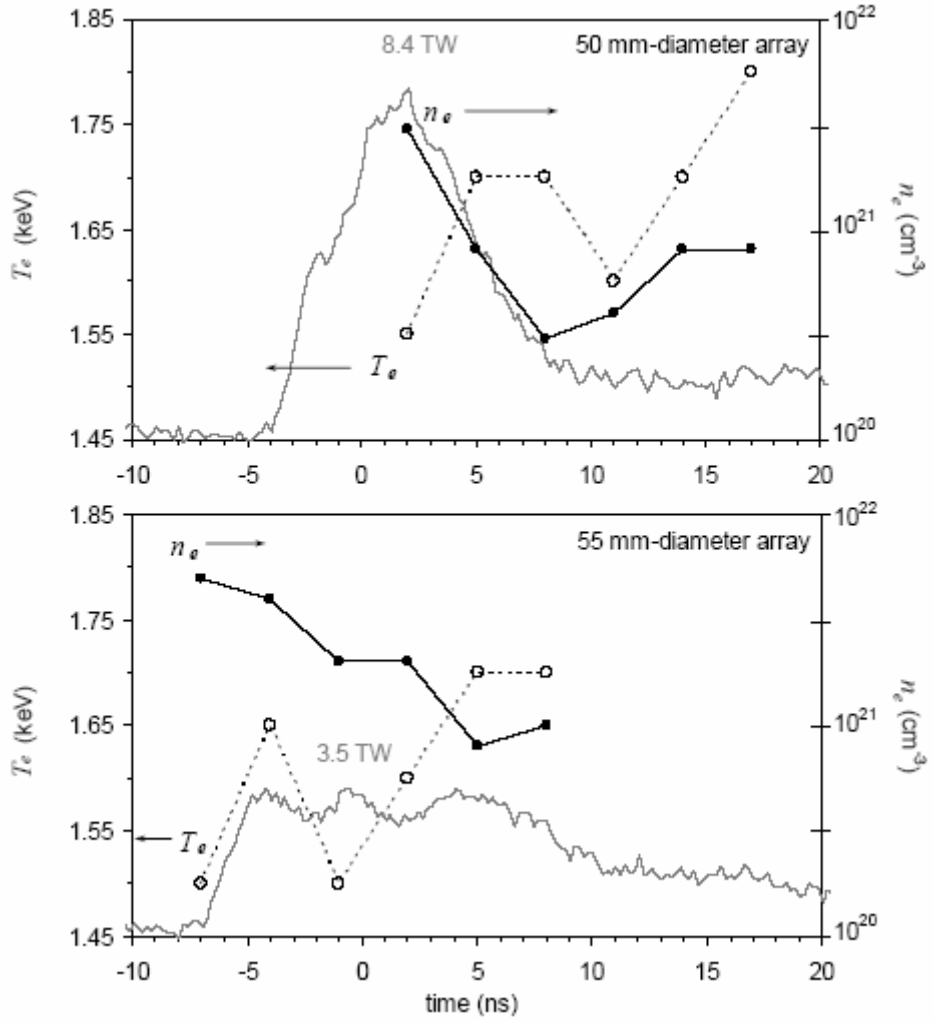

Fig. 13. Time dependence of the diagnosed T_e and n_e from the 50 mm (black lines) and 55 mm (gray lines) wire arrays. Times are relative to the peak total radiated power from each array.